The gene encoding complement factor H lies in the chromosome 1q25-31 region implicated in linkage studies of both a large single family and of multiple small families and sibling pairs. One study suggested that this gene might account for as much as 50% of the hereditary tendency of AMD in the general population (Edwards *et al.*, 2005). In addition, the biochemical activities of both APOE and HF1 are consistent with the proposed atherosclerotic and inflammatory associations of AMD and the histological and biochemical analysis of the subretinal deposits. Thus, significant progress is being made in understanding the biological nature of the genes associated with macular degenerations and their roles in the disease. However, despite these advances little is understood about the overall mechanism underlying the disease process.

BIOCHEMISTRY AND PATHOLOGY OF MACULAR DEGENERATION

Histological changes

Among the early hallmarks of AMD are drusen, which are complex deposits of lipids, proteins, glycoproteins, and glycosaminoglycans that accumulate in the extracellular and inner aspects of Bruch's membrane (Anderson *et al.*, 2002). These subretinal deposits, accompanied by a diffuse thickening of Bruch's membrane, have been speculated to form a physical barrier between the RPE and choroid, obstructing the flow of nutrients from choroid to RPE, or possibly resulting in loss of cell-cell contact between RPE and Bruch's membrane and causing degeneration of retinal tissue. The RPE cells are responsible for phagocytosis and degradation of outer segment disks shed by photoreceptors. As they age and undergo oxidative stress, lipofuscin accumulates in the lysosomal compartment and leads to cellular damage and further impaired function. Though the origin of drusen remains controversial, current opinions are beginning to favor the vasculature of the choriocapillaris as a primary source rather than an intracellular source from the RPE. It is possible that the presence of lipofuscin and cellular debris excites an immune reaction and leads to the formation of drusen. This is reflected by the presence of immune components in drusen (Anderson *et al.*, 2002; see later).

Chorioretinal neovascularization (CNV) is the most common cause of vision loss in AMD. New vessels from the choriocapillaris grow through Bruch's membrane and branch horizontally through the RPE cell layer (termed classic CNV) or between the inner Bruch's membrane and RPE (termed occult CNV because it doesn't show up on angiography). Although the impetus for CNV has not been definitively determined, there are suggestions that imbalances in growth factors include pigment epithelial derived factor (PEDF, which inhibits vascular outgrowth) and vascular endothelial growth factor (VEGF, which stimulates vascular growth), possibly as a result of hypoxia and inflammation of the RPE. Even in the absence of CNV, the changes to the RPE Bruch's membrane and the outer plexiform layer of the retina result in scar formation at that level with concomitant damage to the neurosensory outer retina, termed geographic atrophy, which can also result in loss of central vision.

Composition of drusen and its implications

Understanding the composition of drusen provides important clues to the molecular pathology of the disease. In addition to classical immunohistochemical techniques, several advanced proteome analysis tools have begun to provide detailed information about the nature and composition of drusen. Perhaps the most significant of the new findings is that drusen contain protein molecules that mediate inflammatory and immune processes. These include immunoglobulins, components of complement pathway, and modulators for complement activation (e.g. vitronectin, clusterin, membrane cofactor protein, and complement receptor-1), molecules involved in the acute-phase response to inflammation (e.g. amyloid P component, α1-antitrypsin, and apolipoprotein E), major histocompatibility complex class II antigens, and HLA-DR antigens (Crabb *et al.*, 2002). Cellular components also have been identified in drusen, including RPE debris, lipofuscin, and melanin, as well as processes of choroidal dendritic cells, which are felt to contribute to the inflammatory response (Mullins *et al.*, 2000).

In addition to immune components, a number of other proteins occur in drusen, some of them also found in atherosclerotic plaques and other age-related diseases in which protein deposits occur. The most common of these appear to be TIMP-3, clusterin, vitronectin, and serum albumin. Other proteins found in drusen include serum amyloid P component, apolipoprotein E, IgG, Factor X, and some complement proteins (Mullins *et al.*, 2000). A number of proteins are found exclusively or in increased amounts in drusen associated with AMD than in drusen from individuals unaffected by AMD. These include some crystallins, EEFMP1, and amyloid-beta. In addition, the presence of immunoreactive proteins and oxidative modifications of many proteins found in drusen implicate both oxidation and immune functions in the pathogenesis of AMD.

Immune aspects

These findings have led to the suggestion that immune complex-mediated inflammation damages RPE cells, and choroidal dendritic cells are activated and recruited by injured RPE, whereas RPE cells respond to control dendritic cell activation by secreting proteins that modulate the immune response. Shed or phagocytosed cell membranes of injured RPE or dendritic cells are postulated to function as cores for these secreted components to accumulate and form extracellular deposits.

Furthermore, the codistribution of IgG and terminal complement complexes in drusen implicates an immune response directed against retinal antigens, and the immune complex formation might be taking place at the site of drusen formation. This hypothesis is supported by the presence of putative anti-retinal autoantibodies in the sera of patients with ARMD. Anti-retinal autoantibodies previously have been reported in a number of ocular disorders, including retinitis pigmentosa, paraneoplastic retinopathies, and retinal vasculitis (Anderson *et al.*, 2002). In addition, patients with membranoproliferative glomerulonephritis, in which complement activation and immune complex deposition cause glomerular injury, develop drusen deposits resembling those in ARMD in ultrastructure and composition including C5 and IgG. However, the role of antiretinal autoantibodies in the pathogenesis of ARMD has not been examined in detail. It remains unknown whether the initiation of chronic inflammation and subsequent drusen formation requires autoimmune-mediated events as a primary factor. To clarify the role of autoimmunity, immunogenic molecules for circulating antiretinal autoantibodies in patients need to be identified.

Oxidative aspects

Oxidative damage is implicated in the pathogenesis of AMD by both theoretical considerations and experimental data (Roth, Bindewald, and Holz, 2004). The retina has a highly active metabolism with a resultant high oxygen demand, and is exposed to light and polyunsaturated fatty acids, all of which tend to increase its susceptibility to photo-oxidative damage. In a fashion somewhat analogous to that seen in the lens, as the retina ages its antioxidant defenses begin to decline, here including both antioxidant enzymes and antioxidants such as lutein, and macular pigment density. As the RPE age oxidation of lipids and other cellular components result in accumulation of nonmetabolizable material as lipofuscin in the lysosomes, leading to their enlargement and formation of lipofuscin granules. These closely parallel drusen formation in time and distribution in the retina. In addition, epidemiological correlation of AMD with light exposure, age, and light pigmentation as well as the prevention or delay of AMD by antioxidant vitamins in the AREDS trial also support an oxidative role in AMD.

ANIMAL MODELS OF MACULAR DEGENERATION

Overview

Limited access to appropriate biological materials, especially eye samples from affected donors at different stages of the disease, are an absolute necessity to study mechanisms underlying the macular degenerations. Because it is nearly impossible to obtain these human retinal tissues from patients or from normal controls, animal models play a crucial role for investigating the biological pathway of disease development and for testing therapeutic strategies. Because age-related macular degeneration shares phenotypic similarities with monogenic macular degenerations, manipulation of these genes associated with monogenic macular degenerations to develop transgenic mouse models has been popular. Over the past few years, genetic engineering technologies has allowed the generation of a rapidly growing number of animal models for retinal diseases (Chader, 2002). Animal models have been used to investigate potentially protective therapeutic agents to treat photoreceptor degeneration, stem cell technology, or to test somatic gene therapy strategies (Ali *et al.*, 2000). They are also valuable for studying environmental effects like diet or light on the degeneration process. The animals that have been used to evaluate therapeutic strategies involve rodents, rabbits, pigs, and dogs. However, macula is found only in primates and birds; a monkey model with macular degeneration would be extremely valuable as they not only have a defined macula, but they are also evolutionarily close to humans.

Macular degeneration in monkeys was first described by Stafford in 1974 (Stafford, Anness, and Fine, 1984). He reported that 6.6 % of elderly monkeys showed pigmentary disorders and/or drusen-like spots. El-Mofty and colleagues reported 50% incidence of maculopathy in a rhesus monkey colony at the Caribbean Primate Research Center of the University of Puerto Rico in 1978. The following report from the center indicated that specific maternal lineages had a statistically significant higher prevalence of drusen. Suzuki *et al.*, have described a cynomolgus monkey (*Macaca fascicularis*) colony at the Tsukuba Primate Research Center (Tsukuba city, Japan) with a high incidence of macular degeneration and its pattern of inheritance (Umeda *et al.*, 2005).

Several other naturally occurring animal models have been described for retinal diseases. Rodents, mainly mice, are the most popular animal models as maintenance is less expensive compared to larger animals. However, a low cone:rod ratio and lack of a macula make mice less suitable for studying cone diseases and macular degenerations. Although the pathology in human ARMD is pronounced in the macula area, it is not confined to this central region alone. Abnormal accumulation of drusen and progressive degeneration of the retina, RPE, and underlying choroid characteristics were observed in mouse models generated by candidate gene manipulation or senescence acceleration (Ambati *et al.*, 2003). Choroidal neovascularization also has been described in naturally occurring mouse models. These observations suggest that the lack of a macula in mice may not be a disadvantage when considering the advantages of using the mouse as a model for studying macular degenerations with drusen.

Although monkey models are extremely important for macular degeneration study, there are limitations

using nonhuman primates as animal models, such as longer gestation and life span, slow rate of expanding the pedigree, and cost of maintenance. These limitations can be overcome only by utilizing the mouse model parallel to the monkey model. One such model is a mouse line expressing an inactive form of cathepsin D. The impaired enzymatic activity affects phagocytosis of photoreceptor outer segments in the RPE cells and the mice demonstrate basal laminar and linear deposits.

Animal model of early and late onset macular degeneration monkey

In 1986, a single cynomolgus monkey (*Macaca fascicularis*) with heavy drusen was found in Tsukuba Primate Research Center. After 19 years of mating experiments, that single pedigree has grown to having 57 affected and 182 unaffected monkeys. Macular changes are observed as early as two years after birth, with basal laminar deposits first appearing in the macular region and progressing toward the peripheral retina throughout the lifetime (see Figure 68.4). In all the cases examined no abnormalities were found in the optic disc, retinal blood vessels, or choroidal vasculatures. The affected monkeys share phenotypic similarities with the early stages of ARMD, such as drusen and accumulation of lipofuscin. The immunohistochemical and proteome analysis of drusen in these monkeys share significant similarity with composition of age-related macular degeneration monkeys and also with previously reported human drusen composition. The meaning of this observation is that early onset monkeys produce the same drusen as ARMD patients at accelerated rate of 25 times. Thirteen human candidate gene loci have been excluded by linkage and haplotype analysis. Therefore, the gene associated with macular degeneration in these monkeys is likely to be novel and the genes involved in causing drusen phenotype in humans and monkeys could be either the same or belong to the same biological pathway.

Studies involving early-onset and late-onset macular degeneration monkeys present a unique opportunity to study two independent target points in the biological pathway of retinal tissue that lead to degeneration of the macula at different stages of life. The gene associated with monkey macular degeneration is likely to be a novel gene as we have excluded most of the known macular degeneration loci. Cloning of the monkey macular degeneration gene will allow us to study the biological processes causing degeneration of retina. Due to high conservation between human and macaque genomes, genes associated with macular degeneration in monkeys should possibly play a key role in maintaining the normal function of retina in humans and is likely to be associated with macular degeneration in humans. Although some of the monogenic macular degeneration genes are not associated with ARMD, the phenotype observed in monkeys strongly suggests that this gene may play a role in human ARMD, and this cannot be established until validated by screening patients with ARMD. Understanding the mechanism underlying macular degeneration in these monkeys will enhance our understanding of the disease, identify clinical or molecular markers for early detection, and provide critical information needed to develop therapies for these diseases.

Progressive Open Angle Glaucoma (POAG)

BRIEF OVERVIEW

Epidemiology of POAG

Primary open angle glaucoma is a major cause of blindness throughout the world, affecting between 1 and 2% of individuals over 40 years of age (Klein *et al.*, 1992). The greatest risk factor for the development of POAG is ocular hypertension, to the extent that an elevated intraocular pressure (IOP) is often incorporated into the definition of glaucoma. In addition, the evidence implicating a genetic influence in glaucoma is very strong, and has been borne out in both model-based and model-free linkage studies. Finally, diabetes and myopia have been suggested to be related to development of POAG, but the evidence for this is inconsistent, although it seems likely that high myopia might contribute to development of POAG.

Pathology and physiology of POAG

Although the etiology and even the pathophysiology of glaucoma are still poorly understood, risk factors for glaucoma can be thought of as including both those in the anterior chamber, which tend to increase intraocular

Figure 68.4 Funduscopic view of the retina in Tsukuba primate model of macular degeneration showing drusen and macular changes.

pressure, and those in the retina and optic nerve, which tend to increase susceptibility to damage from elevated or even normal intraocular pressure. Clinically, glaucoma generally is characterized by excavation of the optic disc as seen on funduscopic examination and visual field defects with elevated intraocular pressure included either as a part of the disease or a risk factor. In a simplified schema, one might think of increased resistance of the trabecular meshwork or Schlemm's canal to outflow of the aqueous humor causing an increase in intraocular pressure, which then acts upon sensitive retinal ganglion cells. These cells then degenerate, resulting in both the increased depth and width of the optic cup and the visual field defects. If the increased pressure is acute as it usually is in juvenile onset glaucoma, this process can be painful, but generally POAG is an insidious disease in which the first recognized symptom may be irreversible visual field changes.

Although primary open-angle glaucoma (POAG) is characterized by visual field loss corresponding to the excavation of the optic disc (see Figure 68.5), it is usually associated with an elevation of the intraocular pressure (IOP) over 21 mmHg. Although the pathogenesis of glaucomatous optic neuropathy is poorly understood, it is generally accepted that the IOP is a major risk factor. By definition, there is no increase in IOP over 21 mmHg at any time in eyes with normal-tension glaucoma (NTG), although it is difficult to rule out fleeting or previous elevations of IOP. IOP is heavily influenced by the inflow and outflow of aqueous humor a plasma filtrate actively generated at stroma of ciliary body and filtered across the blood-aqueous barrier. The aqueous flows from the posterior chamber to the anterior chamber via the pupil and released through two routes the trabecular route and uveoscleral route. Any disturbance in the flow can cause abnormal IOP leading to a death of retinal ganglion cells (RGC), and damage to the surrounding structure of the optic nerve head where optic nerve fibers leave the eye for visual cortex.

HUMAN STUDIES OF POAG

Linkage studies

At least six loci for autosomal dominant POAG have been mapped through linkage studies, termed GLC1A-F, on chromosomes 1q23, 2cen-q13, 3q21-q24, 8q23, 10p15-p14, and 7q35-q36. A genome wide scan in multiple small families from an Afro-Caribbean population provided significant evidence for linkage to regions on chromosomes 2q (but separate from the Mendelian POAG locus GLC2B and the infantile glaucoma locus GLC3A on chromosome 2) and 10p. Presumably, these represent loci for glaucoma risk factors common in the general population, as do the loci on chromosomes 2, 14, 17, and 19 identified by examining siblings in an American population of European descent. It is particularly important to note that few of these studies have been confirmed; especially the technically more difficult and laborious studies of POAG in the general population.

Association studies

In addition to the identification of myocilin as a causative gene in glaucoma described earlier, which was carried out by linkage studies primarily in families with juvenile glaucoma and very elevated intraocular pressure, association studies have identified sequence changes in myocilin as a risk factor in a small percentage of POAG cases. Two additional genes have been shown to be involved in glaucoma by demonstrating an association between sequence changes in those genes and glaucoma in population studies. One of these genes is optineurin, for which the strongest associations have been obtained with normal tension glaucoma, but which also might be associated with POAG in some populations. A second is the OPA1 gene, which is known primarily as a cause of optic atrophy, but is also associated with normal tension glaucoma but not with high tension primary open angle glaucoma in most studies. Association of both these genes with normal tension glaucoma suggests that

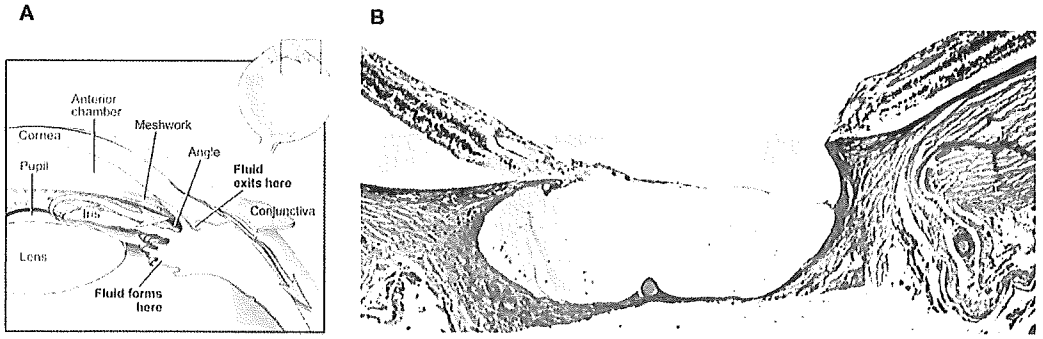

Figure 68.5 A. Diagram depicting the flow of aqueous humor from synthesis in the ciliary body to exit from the anterior chamber through the trabecular meshwork and Schlem's canal. B. Histological section showing an excavated optic cup in an individual with glaucoma. Courtesy of Dr. Chi Chao Chan, National Eye Institute, National Institutes of Health, from the collection of Dr. W. R. Green.

there may be some relationship between normal tension glaucoma and optic atrophy, and also emphasizes the importance of genetic changes that sensitize the retina and optic nerve to minor elevations of or even normal intraocular pressure.

BIOCHEMISTRY AND PATHOLOGY OF POAG

Histological changes

It is estimated that roughly 20 to 50% of the large retinal ganglion cells (RGC) are lost in POAG. Although the reduction of RGC density occurs equally throughout the retina, visual sensitivity is first lost in areas where the initial RGC density is low, especially in the peripheral regions of the retina. As the disease progresses, atrophy of the nerve fiber layer usually observed as additional RGC are lost. Typically, vertical collapse of the optic nerve head (ONH), loss of the neural rim at the ONH, rearrangement of central blood vessels, and loss of supporting tissue occur. Scanning electron microscopy of retinas with early stages of glaucoma shows evidence of initial collapse of the anterior lamina cribrosa, primarily in the vertical poles of the optic nerve head. Based on primate studies optic cups with larger diameters are more susceptible to high ocular pressure and thus to glaucoma.

Role of the trabecular meshwork

Trabecular meshwork (TM) is a lamellated sheet of complex tissue that covers the inner wall of Schlemm's canal. TM has uniquely developed at the angle of primates, filtering the aqueous humor out of the eye. TM consists of two parts the nonfiltering portion mainly occupied by trabecular cells and filtering portion. Trabecular cells are highly phagocytic cells removing particles, cells debris, and protein from the aqueous humor. The first glaucoma locus, the *trabecular meshwork inducible glucocorticoid response* (TIGR), also known as myocilin, initially was identified by looking at genes whose transcription is highly induced by steroids in these cells. The filtering portion consists of three tissues: the cribriform layer, the corneoscleral meshwork, and the uveal meshwork. These trabecular beams or strands are intertwiningly connected to each other, forming a complex filtering mesh surrounding Schlemm's canal. The trabecular beams are thickened by accumulation of extracellular materials and decrease of cell density within the corneoscleral and uveal meshwork decreases in aged eyes.

ANIMAL MODELS OF POAG

Overview: Difficulty of modeling the human eye

Limited access to appropriate biological materials, especially eye samples from affected donors at different stages of the POAG, is an impediment to the study of mechanisms underlying the disease. Because of the extreme difficulty in obtaining such diseased eyes from both patients and normal controls, animal models play a crucial role in investigating the biological pathway of disease development and in testing therapeutic strategies.

Different types of animal models for POAG have been found or created to mimic the optic nerve damage to resemble POAG phenotype in human. The greatest difficulty in constructing an animal model for POAG lies in the diversity of the anterior structures of the eye among different species (Tripathi and Tripathi, 1972; 1973). These structural differences include different iridocorneal angles or absence of specific quadrants from the TM. Nevertheless, within the limited areas in which interpretation of the data from a specific animal model parallels that in the human, various animals including the cow, dog, cat, horse, rabbit, chicken, and monkey can be used to observe POAG under various experimental conditions.

Animal models of POAG

Various animal models for inducible glaucoma have been reported. Argon laser photocoagulation of the TM in rhesus monkeys results in sustained elevation of IOP and has been used extensively to study early damage to the optic nerve head (May *et al.*, 1997). Corticosteroids such as betamethasone and dexamethasone have been used to treat rabbits, dogs, and cats to develop ocular hypertension (Bonomi *et al.*, 1978). Steroid treatment generally produces progressive glaucoma, but this process is reversed after about two months after cessation of the steroid. Trabecular blockage caused by inflammation after of α-chymotrypsin treatment also has been used to produce elevated IOP in rabbit and monkey eyes (Vareilles *et al.*, 1977). Some types of avian species (chicken, quail, and turkey) have been known to develop elevated IOP as a consequence of continuous exposure to light.

Mouse models of glaucoma

Naturally occurring inherited animal glaucoma models are rare. However, extensive classification of IOP in mouse strains and molecular biological techniques to manipulate certain genes to produce transgenic or knockout/knockin mice recently have resulted in the development of a number of animal models with definitely known genetic causes for their disease (Chang *et al.*, 1999). As discussed earlier, four genes, myocilin (*MYOC, TIGR*), cytochrome P4501B1 (*CYP1B1*), optineurin (*OPTN*), and WDR36, currently are associated with glaucoma. OPTN, mutations of which are responsible for 16.7% of families with hereditary human NTG, is homologous to an inhibitory regulatory subunit of the high molecular kinase complex for the phosphorylation of NF-κB. Some of its known functions include inhibition of the tumor necrosis factor-alpha pathway, interaction with transcription factor IIIA, and mediation of the Huntington and Rab8 interaction for regulation of

membrane trafficking and cellular morphogenesis. OPTN is induced by TNF-α and binds to an inhibitor of TNF-α and the adenovirus E3-14.7 kDa protein. To determine the effects of human glaucoma mutations in a transgenic mouse system, mice over-expressing wild type OPTN, OPTN carrying the glaucoma associated mutation E50K, and OPTN with exon5 deleted were constructed. Although wild type OPTN do not show any abnormalities and the exon 5 deleted construction was found to be lethal prenatally, mice transgenic for the E50K mutant OPTN show steep optic nerve cupping with rearrangement of supporting tissue and blood vessel 18 weeks after birth (see Figure 68.6). The RGC and astrocyte loss observed is similar to the end phase changes seen in human glaucoma patients. Understanding the mechanism underlying normal tension glaucoma in these transgenic mice will enhance our understanding of each step leading to optic nerve cupping and how to prevent it. Based on the success of the mouse model, use of larger animals such as transgenic rabbits or pigs, in which more precise measurement of IOP and trials of surgical procedures suitable for therapy in humans are possible are currently being investigated.

Other glaucoma mouse models have been made through genetic manipulation. Knockout and transgenic mouse model of myocilin were made to answer the question whether elevated expression of the myocilin protein can influence the IOP (Gould *et al.*, 2004). Up to a fifteen-fold increase in myocilin expression failed to result in elevation of the IOP, any abnormality of retinal ganglion cells, or cupping of the optic nerve head. Mice lacking the cytochrome P450 1B1 (CYP1B1) gene were generated on B6 and 129X1/SvJ mouse stains (Libby *et al.*, 2003). Both strains were affected by the CYP1B1 deficiency with focal angle abnormalities but 129X1/SvJ albino strain lacking tyrosinase were more severely affected, suggesting the presence of tyrosinase as an important developmental molecule.

Figure 68.6 Histological section demonstrating excavation of the optic disc in an 18 week old E50K mutant OPTN transgenic mouse.

Conclusion

In this chapter we have provided a brief overview of age-related eye diseases and the current state of knowledge and research on three of these. Age-related cataracts, age-related macular degeneration, and progressive open angle glaucoma account for much of the population burden imposed by age-related eye diseases. Although no perfect system to study these diseases exists today, an increasing number of experimental models are being developed. Although none is an exact replica of the clinical disease and should not be applied indiscriminately, each of these can provide useful information on some aspects of the disease in humans. They promise to accelerate the pace of research and provide mechanistic and therapeutic insights into the diseases that threaten sight in our aging population.

Recommended Resources

Albert, D.M. and Jakobiec, F.A. (Eds.) (2000). *Principles and Practice of Ophthalmology, 2e.* Philadelphia: W.B. Saunders Co.

Scriver, C.R. *et al.* (Eds.) (2005). *The Metabolic and Molecular Bases of Inherited Disease*, 8e. New York: McGraw-Hill.

Tasman, W. and Jaeger, E. (Eds.) (2001). *Duane's Clinical Ophthalmology.* Philadelphia: J.B. Lippincott Co.

REFERENCES

Ali, R.R., Sarra, G.M., Stephens, C., Alwis, M.D., Bainbridge, J.W., Munro, P.M. *et al.* (2000). Restoration of photoreceptor ultrastructure and function in retinal degeneration slow mice by gene therapy. *Nat. Genet.* 25 (3), 306–310.

Ambati, J., Anand, A., Fernandez, S., Sakurai, E., Lynn, B.C., Kuziel, W.A. *et al.* (2003). An animal model of age-related macular degeneration in senescent Ccl-2- or Ccr-2-deficient mice. *Nat. Med.* 9 (11), 1390–1397.

Anderson, D.H., Mullins, R.F., Hageman, G.S., and Johnson, L.V. (2002). A role for local inflammation in the

formation of drusen in the aging eye. *Am. J Ophthalmol.* 134 (3), 411–431.

Bonomi, L., Perfetti, S., Noya, E., Bellucci, R., and Tomazzoli, L. (1978). Experimental corticosteroid ocular hypertension in the rabbit. *Albrecht. Von. Graefes Arch. Klin. Exp. Ophthalmol.* 209 (2), 73–82.

Brady, J.P., Garland, D., Duglas-Tabor, Y., Robison, W.G. Jr., Groome, A., and Wawrousek, E.F. (1997). Targeted disruption of the mouse alpha A-crystallin gene induces cataract and cytoplasmic inclusion bodies containing the small heat shock protein alpha B-crystallin. *Proc. Natl. Acad. Sci. USA* 94, 884–889.

Buch, H., Vinding, T., La Cour, M., Appleyard, M., Jensen, G.B., and Nielsen, N.V. (2004). Prevalence and causes of visual impairment and blindness among 9980 Scandinavian adults: The Copenhagen City Eye Study. *Ophthalmology* 111 (1), 53–61.

Chader, G.J. (2002). Animal models in research on retinal degenerations: Past progress and future hope. *Vision Res.* 42 (4), 393–399.

Chang, B., Smith, R.S., Hawes, N.L., Anderson, M.G., Zabaleta, A., Savinova, O. *et al.* (1999). Interacting loci cause severe iris atrophy and glaucoma in DBA/2J mice. *Nat. Genet.* 21 (4), 405–409.

Congdon, N.G., Friedman, D.S., and Lietman, T. (2003). Important causes of visual impairment in the world today. *J.A.M.A.* 290 (15), 2057–2060.

Crabb, J.W., Miyagi, M., Gu, X., Shadrach, K., West, K.A., Sakaguchi, H. *et al.* (2002). Drusen proteome analysis: An approach to the etiology of age-related macular degeneration. *Proc. Natl. Acad. Sci. USA* 99 (23), 14682–14687.

Davies, M.J. and Truscott, R.J. (2001). Photo-oxidation of proteins and its role in cataractogenesis. *J. Photochem. Photobiol. B* 63 (1–3), 114–125.

Edwards, A.O., Ritter, R. III, Abel, K.J., Manning, A., Panhuysen, C., and Farrer, L.A. (2005). Complement factor H polymorphism and age-related macular degeneration. *Science* 308 (5720), 421–424.

Giblin, F.J., Padgaonkar, V.A., Leverenz, V.R., Lin, L.R., Lou, M.F., Unakar, N.J. *et al.* (1995). Nuclear light scattering, disulfide formation and membrane damage in lenses of older guinea pigs treated with hyperbaric oxygen. *Exp. Eye Res.* 60 (3), 219–235.

Gould, D.B., Miceli-Libby, L., Savinova, O.V., Torrado, M., Tomarev, S.I., Smith, R.S. *et al.* (2004). Genetically increasing Myoc expression supports a necessary pathologic role of abnormal proteins in glaucoma. *Mol. Cell Biol.* 24 (20), 9019–9025.

Graw, J. and Loster, J. (2003). Developmental genetics in ophthalmology. *Ophthalmic Genet.* 24 (1), 1–33.

Hammond, C.J., Webster, A.R., Snieder, H., Bird, A.C., Gilbert, C.E., and Spector, T.D. (2002). Genetic influence on early age-related maculopathy: a twin study. *Ophthalmology* 109 (4), 730–736.

Hanson, S.R., Hasan, A., Smith, D.L., and Smith, J.B. (2000). The major in vivo modifications of the human water-insoluble lens crystallins are disulfide bonds, deamidation, methionine oxidation and backbone cleavage. *Exp. Eye Res.* 71 (2), 195–207.

Heiba, I.M., Elston, R.C., Klein, B.E., and Klein, R. (1994). Sibling correlations and segregation analysis of age-related maculopathy: The Beaver Dam Eye Study. *Genet. Epidemiol.* 11 (1), 51–67.

Hejtmancik, J.F., Kaiser-Kupfer, M.I., and Piatigorsky, J. (2001). Molecular biology and inherited disorders of the eye lens. In C.R. Scriver *et al.* (Eds.). *The Metabolic and Molecular Basis of Inherited Disease, 8e.* New York: McGraw Hill.

Hejtmancik, J.F. and Kantorow, M. (2004). Molecular genetics of age-related cataract. *Exp. Eye Res.* 79 (1), 3–9.

Hejtmancik, J.F. and Smaoui, N. (2003). Molecular Genetics of Cataract. In B. Wissinger, S. Kohl, and U. Langenbeck (Eds.). *Genetics in Ophthalmology.* Basel: S. Karger.

Klein, B.E., Klein, R., Sponsel, W.E., Franke, T., Cantor, L.B., Martone, J. *et al.* (1992). Prevalence of glaucoma. The Beaver Dam Eye Study. *Ophthalmology* 99 (10), 1499–1504.

Kuck, J.F. (1990). Late onset hereditary cataract of the Emory mouse. A model for human senile cataract. *Exp. Eye Res.* 50, 659–664.

Libby, R.T., Smith, R.S., Savinova, O.V., Zabaleta, A., Martin, J.E., Gonzalez, F.J. *et al.* (2003). Modification of ocular defects in mouse developmental glaucoma models by tyrosinase. *Science* 299 (5612), 1578–1581.

May, C.A., Hayreh, S.S., Furuyoshi, N., Ossoinig, K., Kaufman, P.L., and Lutjen-Drecoll, E. (1997). Choroidal ganglion cell plexus and retinal vasculature in monkeys with laser-induced glaucoma. *Ophthalmologica* 211 (3), 161–171.

McCarty, C.A. and Taylor, H.R. (2001). The genetics of cataract. *Invest Ophthalmol. Vis. Sci.* 42 (8), 1677–1678.

Mullins, R.F., Russell, S.R., Anderson, D.H., and Hageman, G.S. (2000). Drusen associated with aging and age-related macular degeneration contain proteins common to extracellular deposits associated with atherosclerosis, elastosis, amyloidosis, and dense deposit disease. *FASEB J.* 14 (7), 835–846.

Okano, Y., Asada, M., Fujimoto, A., Ohtake, A., Murayama, K., Hsiao, K.J. *et al.* (2001). A genetic factor for age-related cataract: identification and characterization of a novel galactokinase variant, "Osaka," in Asians. *Am. J. Hum. Genet.* 68 (4), 1036–1042.

Roth, F., Bindewald, A., and Holz, F.G. (2004). Key pathophysiologic pathways in age-related macular disease. *Graefes Arch. Clin. Exp. Ophthalmol.* 242 (8), 710–716.

Seddon, J.M., Ajani, U.A., and Mitchell, B.D. (1997). Familial aggregation of age-related maculopathy. *Am. J. Ophthalmol.* 123 (2), 199–206.

Spector, A. (1995). Oxidative stress-induced cataract: mechanism of action. *FASEB J.* 9 (12), 1173–1182.

Stafford, T.J., Anness, S.H., and Fine, B.S. (1984). Spontaneous degenerative maculopathy in the monkey. *Ophthalmology* 91 (5), 513–521.

The Italian-American Cataract Study Group (1991). Risk factors for age-related cortical, nuclear, and posterior subcapsular cataracts. *Am. J. Epidemiol.* 133, 541–553.

Thylefors, B., Negrel, A.D., Pararajasegaram, R., and Dadzie, K.Y. (1995). Global data on blindness. *Bull. World Health Organ.* 73 (1), 115–121.

Tripathi, R.C. and Tripathi, B.J. (1972). The mechanism of aqueous outflow in lower mammals. *Exp. Eye Res.* 14 (1), 73–79.

Tripathi, R.C. and Tripathi, B.J. (1973). The mechanism of aqueous outflow in birds. I. An ultrastructural study of normal eyes. *Exp. Eye Res.* 15 (3), 409–423.

Tuo, J., Bojanowski, C.M., and Chan, C.C. (2004). Genetic factors of age-related macular degeneration. *Prog. Retin. Eye Res.* 23 (2), 229–249.

Umeda, S., Ayyagari, R., Okamoto, H., Suzuki, M.T., Terao, K., Mizota, A. *et al.* (2005). Linkage and mutation analysis to identify the gene associated with macular degeneration segregating in a cynomolgus monkey. *Invest. Ophthalmol. Vis. Sci.* 46, 683–691.

Vareilles, P., Silverstone, D., Plazonnet, B., Le Douarec, J.C., Sears, M.L., and Stone, C.A. (1977). Comparison of the effects of timolol and other adrenergic agents on intraocular pressure in the rabbit. *Invest. Ophthalmol. Vis. Sci.* 16 (11), 987–996.

（財）政策医療振興財団の助成による研究報告

網膜色素上皮細胞増殖因子 REF-1の機能解析

独立行政法人国立病院機構
東京医療センター　薬剤科
主任研究者　渋　谷　昌　彦

共同研究者

独立行政法人国立病院機構東京医療センター
臨床研究センター　細胞・分子生物学研究室　　岩　田　　岳

網膜色素上皮（Retinal pigment epithelial：RPE）細胞は、網膜の恒常性を維持し、視細胞と脈絡膜毛細血管の栄養交換や視細胞外節の貪食等の重要な役割を果たすことが知られている。そこでこのRPE細胞の機能低下や消失を治療するために、我々はRPE細胞の増殖を特異的に促進する因子の検索を行った。その結果、サイトカインや増殖因子を豊富に生成する繊維芽細胞抽出液中にRPE細胞の特異的な増殖機能を持つ増殖因子を発見し、Retinal pigment epithelial cell Factor-1（REF-1）と命名した。そのREF-1の添加によって、どのようにRPE細胞が増殖し、なぜ増殖が促進されるのかを明らかとするために、今回、RPE細胞培養の条件を検討し、RPE細胞におけるREF-1の発現とREF-1添加による成長因子やサイトカインの分泌、さらにRPE細胞内での遺伝子発現の変動を解析した。

実験方法

培養細胞はhuman primary RPE (passage 4)、培養液は15%Fetal bovine serum（FBS）を加えたDulbecco's modified Eagle medium (DMEM)、Plateはコラーゲンコートの24well plateを用いて、1wellあたり2.5×10^4 cells/0.5 mL medium/wellとなるように播種した。培養温度は37度、5 %CO_2下の条件で細胞培養を行った。m-ＲＮＡの発現解析には、human primary RPE細胞からtotal RNAを抽出し、DNase処理後、RT-PCRによってcＤＮＡを作成した。これを更にPCR反応にて増幅し、このPCR溶液を１%アガロースゲルで電気泳動して発現確認を行った。また、REF-1タンパクはWestern Blotにてその発現を確認した。

次に、培養human primary RPE細胞に、REF-1を添加することによって、成長因子とサイトカイン分泌に変動が認められるかを明らかとするために、ELISA kitを用いてその確認を試みた。

更に、培養開始２目のhuman primary RPE（passage 4）細胞に、REF-1を添加し、６時間、12時間、24時間後毎にtotal RNA isolation kit（RNA-Bee-RNA Isolation Reagent; Tel-Test, Friendswood, TX）を用いてtotal RNAを抽出し、DNase処理後、このRNAを用いて、マイクロアレイによる遺伝子の発現解析を行った。今回、遺伝子の発現解析には、Applied Biosystems 1700（AB1700）Chemiluminescent Microarray Analyzerを用いた。また、検出されたREF-1処理と未処理のデータ

間の比較には、Celera Discovery System (Applied Biosystems) を用いて解析を行った。

結　果

RPE細胞の1 wellに播種する密度を変化させることによって、RPE細胞の増殖率に変化のあることがわかった。今回の実験では、24wellのコラーゲンコートプレートの1wellに播種する密度を2.5×10^4細胞とすることで、最も高い増殖率を得られることが分かった。

また、human primary RPE 細胞中にREF-1が存在するのかを明らかとするために行ったRT-PCRと Western blot による確認の結果では、RT-PCRでRPE細胞のtotal RNA中にREF-1のm-RNAの発現を確認することができた。しかし、Western blotの結果では、REF-1のタンパクの発現を確認することはできなかった。

次に、培養細胞にREF-1を加え、無血清培地で2日間培養後、培養上清液を用いて11の成長因子とサイトカインの測定を行った結果は、REF-1を添加することによって、TGF-β1 で4.7倍、GM-CSFで2.4倍の分泌上昇が認められた。またbFGF, IL-6, IL-8, M-CSFでは、わずかな分泌上昇を認めた。そして、今回TGF-β2, IL-1β, G-CSF, TNF-α, EGFを検出することはできなかった。

更に、培養開始2日目にREF-1を添加した後、各6,12,24時間におけるREF-1処理、未処理の検体（n=6）毎にハイブリダイゼーションを行ったマイクロアレイ（シグナルの検出は33,096の全遺伝子で行った。遺伝子の発現はバックグラウンドに比較して、シグナル強度が3倍以上示すものとした。）による遺伝子発現解析の結果は、REF-1処理を行ったものでは10,773の遺伝子の発現を認め、REF-1処理を行わなかったものでは2,186の遺伝子の発現を認めた。また、今回REF-1処理を行わなかったRPE細胞での遺伝子の発現量に対するREF-1処理を行ったRPE細胞における遺伝子の発現量の比（Ratio）を取り、遺伝子発現の変動パターンについてもOmniViz data mining softwareを用いてクラスター解析を試みた。その結果、全遺伝子の時間ごとの発現パターンを38のクラスターに分けたときに、各時間の発現遺伝子に明らかな変化のあることが分かった。

考　察

RPE細胞密度によって、その増殖率に変化はあるが、REF-1を添加することによって、human primary RPE 細胞の増殖を促進することがわかった。そして、RPE細胞でREF-1が独自に供給されているかについては、今回のWestern Blotの結果においてREF-1のタンパクの発現を確認するまでに至らなかったので、明らかではないが、このタンパクの生成に至るためには、RPE細胞中で発現の認められたm-RNAに何らかの特異的な要因が必要なのかもしれない。また、RPE細胞の増殖に関与する他の増殖因子とサイトカインのREF-1添加後の変動について検討を行った結果では、有意にTGFβ1の分泌上昇が認められた。我々は、REF-1の処理によって、急速な増殖過程にあるRPE細胞の増殖を調節もしくは抑制するためにTGFβ1の分泌上昇が、生じているのではないかと考えた。そして、なぜ骨髄細胞系の増殖因子であることが知られているGM-CSFの分泌が上昇したのかについては、今回得られたマイクロアレイの結果解析とともに他の成長因子やサイトカインも含め調査、検討を継続して進めたいと思う。

参考文献

Tanaka Y, et al. Purification, Molecular Cloning, and Expression of a Novel Growth-Promoting Factor for Retinal Pigment Epithelial Cells, REF-1/TFPI-2.Invest Ophthalmol Vis Sci. 2004;45:245-252

Jpn J Ophthalmol 2005;49:281–286

DOI 10.1007/s10384-005-0194-z

LABORATORY INVESTIGATION

Visual Simulation of Retinal Images Through a Decentered Monofocal and a Refractive Multifocal Intraocular Lens

Kazuno Negishi[1], Kazuhiko Ohnuma[2], Takashi Ikeda[3], and Toru Noda[4]

[1]Department of Ophthalmology, Keio University School of Medicine, Tokyo, Japan; [2]Faculty of Engineering, Chiba University, Chiba, Japan; [3]Center for Environmental Remote Sensing, Chiba University, Chiba, Japan; [4]Division of Disability and Rehabilitation Research, National Institute of Sensory Organs, Tokyo, Japan

Abstract

Purpose: To evaluate the effect of decentration of a monofocal intraocular lens (IOL) and a refractive multifocal IOL on retinal image quality using a new visual simulation system.

Methods: Using a new visual simulation system, we performed visual simulation of a monofocal and a multifocal IOL at 5, 4, 3, 2, 1, and 0.4 m with several decentered IOL positions from 0 to 1.0 mm through a 3- or 4-mm aperture using Landolt visual acuity (VA) charts. The VA was estimated under each condition from the simulated retinal image.

Results: With a monofocal IOL, the image was affected minimally by decentration at 4 and 5 m; at 2 and 3 m, the image contrast decreased slightly with increased decentration. With the multifocal IOL, some loss of image contrast developed at all distances compared with the monofocal IOL; however, the images of the Landolt's rings were still recognizable under all conditions.

Conclusions: Our results suggest that up to 1.0 mm of decentration of a monofocal and multifocal IOL would not greatly affect the retinal image quality. **Jpn J Ophthalmol** 2005;49:281–286 © Japanese Ophthalmological Society 2005

Key Words: decentration, intraocular lens, visual simulation

Introduction

Modern intraocular lens (IOL) implantation usually provides good visual results. There have been many reports on the optical performance of different types of monofocal and multifocal IOLs using optical bench testing[1–5] and ray tracing,[6] and there have also been many clinical studies[7–21] of visual performance, mainly visual acuity (VA) and contrast sensitivity, in patients in whom these IOLs have been implanted under various conditions. However, the image quality of IOLs measured by optical bench testing outside the eye and the results of ray tracing are difficult to extrapolate to conditions in a pseudophakic eye in vivo. On the other hand, clinical (psychophysical) tests may be affected by nonoptical factors in the patients' visual system, so that the tests may not reflect the optical performance of the IOL. Therefore, there has not been an appropriate method for evaluating the optical performance of an IOL objectively under the various possible conditions. This indicates the need for a new method of evaluating the retinal image quality in eyes with IOLs under conditions that closely resemble clinical cases.

We previously reported a new system for visual simulation of retinal images in eyes with an IOL under conditions similar to clinical cases and demonstrated the differences in retinal image quality with a monofocal and a multifocal IOL.[1]

Received: November 17, 2004 / Accepted: February 16, 2005
Correspondence and reprint requests to: Kazuno Negishi, Department of Ophthalmology, Keio University School of Medicine, 35 Shinanomachi, Shinjuku-ku, Tokyo 160-8582, Japan.
e-mail: fwic7788@infoweb.ne.jp

Jpn J Ophthalmol
Vol 49: 281–286, 2005

In this study, we carried out visual simulation of retinal images in eyes with a monofocal IOL and a refractive multifocal IOL, with and without decentration, using our new system to evaluate the effect of decentration on optical performance.

Methods

Visual Simulation System

Our system to simulate the retinal image in an eye with an IOL has been described in detail elsewhere.[1] The schema of this system is shown in Fig. 1. The fundamental approach in this system involves simulating retinal images in eyes with an IOL under conditions that closely resemble the actual clinical environment. Our system consists of a photographic lens with a 35-mm focal length (Nikon, Tokyo, Japan), an IOL in a water cell, and a charge-coupled device (CCD) camera (Megaplus, Kodak, Rochester, NY, USA). The photographic lens, which corresponds to the cornea, is placed in front of the water cell that holds the IOL. By adjusting the distance between the photographic lens and the IOL, the incident angle to the IOL from the photographic lens in this system can be set to the same incident angle from the cornea in a human eye. The images formed by the lens can be detected by the CCD camera and observed on the monitor of a personal computer. The aperture diameter, the centering of the IOL position in the optical axis, and the type of IOL are exchangeable in the water cell. Spectacle lenses also can be placed in front of the photographic lens. The different aperture sizes were chosen to allow comparable viewing angles for distance and near-focus testing. The sensitivity of the CCD camera can be adjusted near to that of the retina by a green or infrared cut-off filter in front of the photographic lens. The contrast threshold of the CCD camera is about 0.008, which is close to the contrast threshold (0.01) of a human eye.

IOLs

We used two types of IOLs: a monofocal IOL (PS-54ANB, Advanced Medical Optics, Santa Ana, CA, USA) and a refractive multifocal IOL (PA154N, Advanced Medical Optics). These IOLs have almost the same design, except for the zonal progressive design on the anterior surface of the latter (Fig. 2). The PA154N is a one-piece polymethylmethacrylate IOL with a 6.0-mm round optic and modified C loops with five aspheric annular refractive zones on the anterior surface. The distance power in the annular zone is located centrally, gradually increases in added power up to 3.5 diopters (D) toward the periphery, and then changes power until the end of the zone (Fig. 3). With this design, 60% of the light passes through the distance regions of the IOL, and the remainder is distributed for intermediate and near vision. The optical design and additional power of the PA154N are shown in Fig. 3. Only a specific IOL power can be used in this system, because the power of an IOL is fully

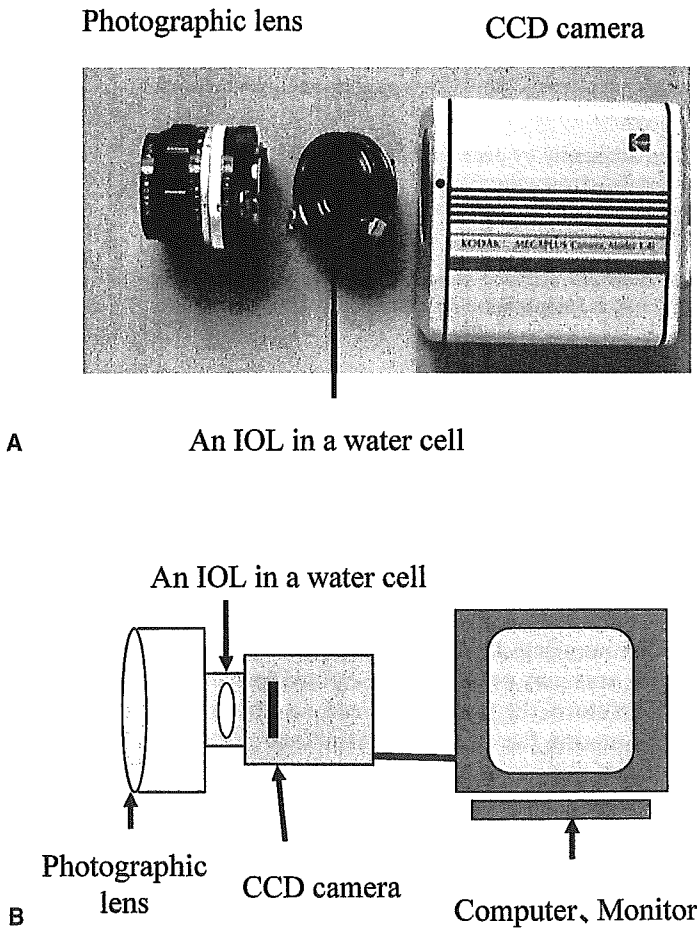

Figure 1A, B. Visual simulation system. **A** Eye model combined with a photographic lens, a water cell, and a charge-coupled device (*CCD*) camera. **B** Schema of visual simulation system. *IOL*, intraocular lens.

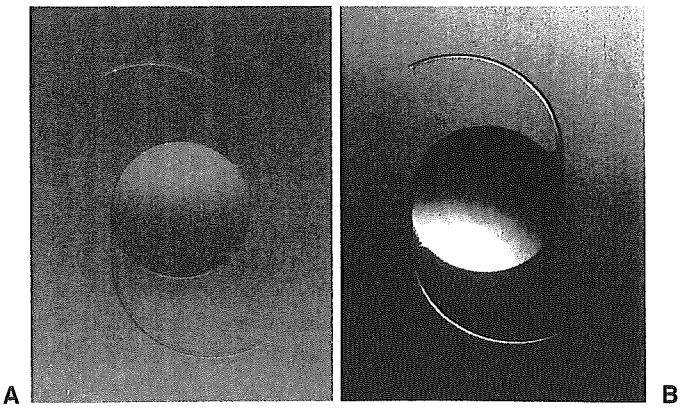

Figure 2A, B. Intraocular lenses. **A** Monofocal IOL (PS54ANB, Advanced Medical Optics); **B** refractive multifocal IOL (PA154N, Advanced Medical Optics).

defined by the power of the photographic lens corresponding to the cornea and the distance corresponding to the axial length. In our study, the power of each IOL was 20 D, and the additional power of the multifocal IOL was 3.5 D.

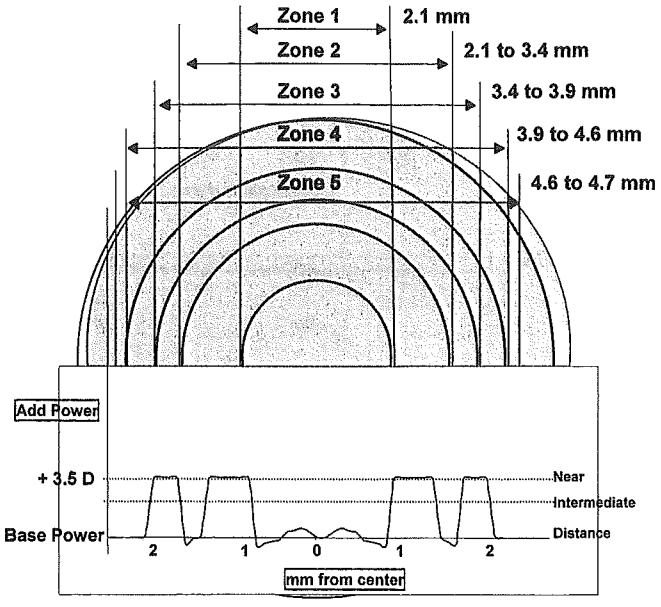

Figure 3. Optic design of PA154N (presented by Advanced Medical Optics).

Examination Settings

Landolt VA charts for examination distances of 5, 4, 3, 2, 1, and 0.4 m were prepared. Visual simulation at each distance was performed with several IOLs decentered from 0 to 1.0 mm through a 3-mm aperture as a small pupil or a 4-mm aperture as a large pupil.

Estimation of VA from Simulated Retinal Images

The angular separation of the gap of a Landolt's ring is 1 minute of arc for 1.0 VA. The VA was estimated according to the hypothesis that a subject can recognize the gap in a Landolt's ring when the contrast of the gap of a simulated retinal image of the Landolt's ring is over 0.8% on the basis of the contrast sensitivity without blurring by the optics of the eye, as reported by Campbell and Green.[22] This contrast threshold is near that of the CCD camera (0.008) and that of a human eye (0.01) under photopic conditions.

Results

Figure 4 shows images of VA charts with a monofocal and a multifocal IOL. With the monofocal IOL, the image quality degraded as the distance decreased. The image was minimally affected by decentration at 4 and 5 m; however, at 2 and 3 m, the image contrast decreased slightly as decen-

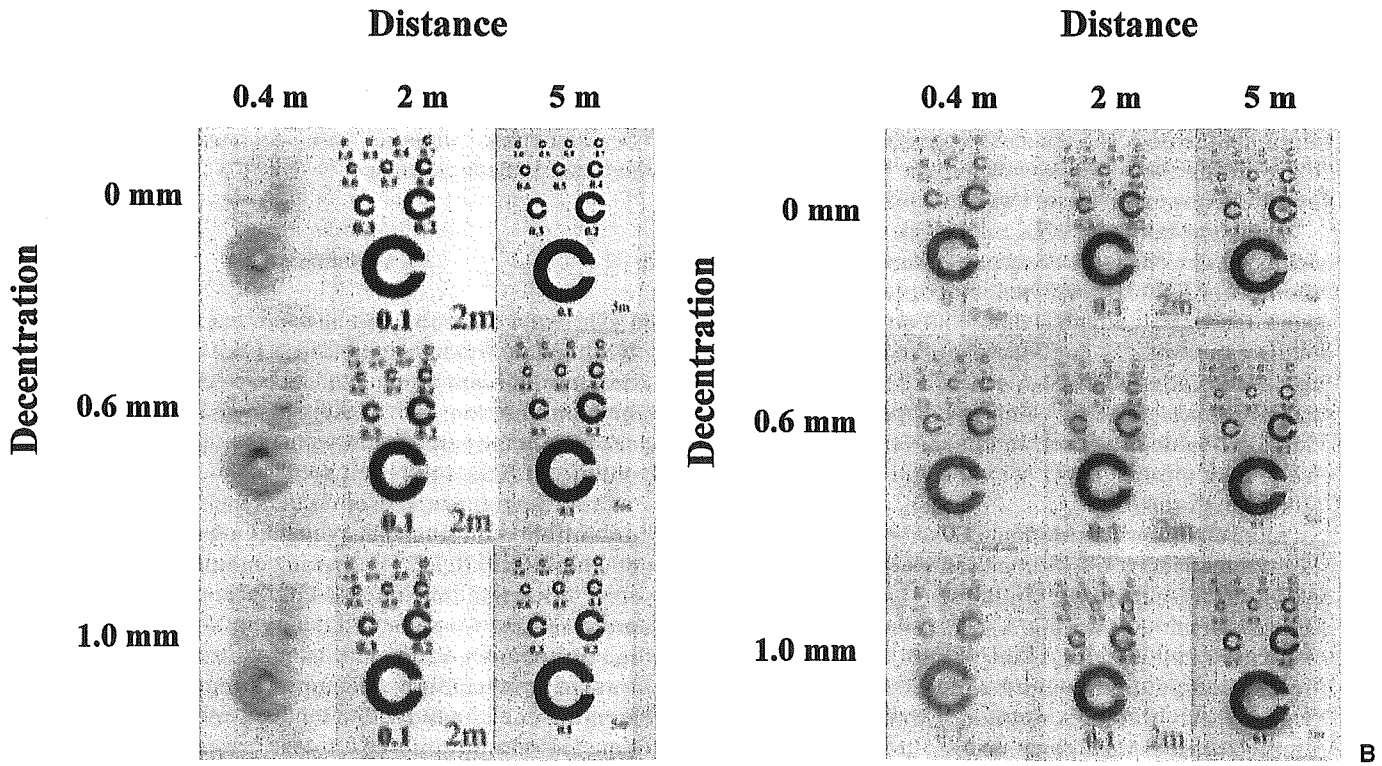

Figure 4A, B. Images of visual acuity charts detected by the CCD camera. **A** Monofocal, φ = 3 mm; **B** multifocal, φ = 4 mm.

Jpn J Ophthalmol
Vol 49: 281–286, 2005

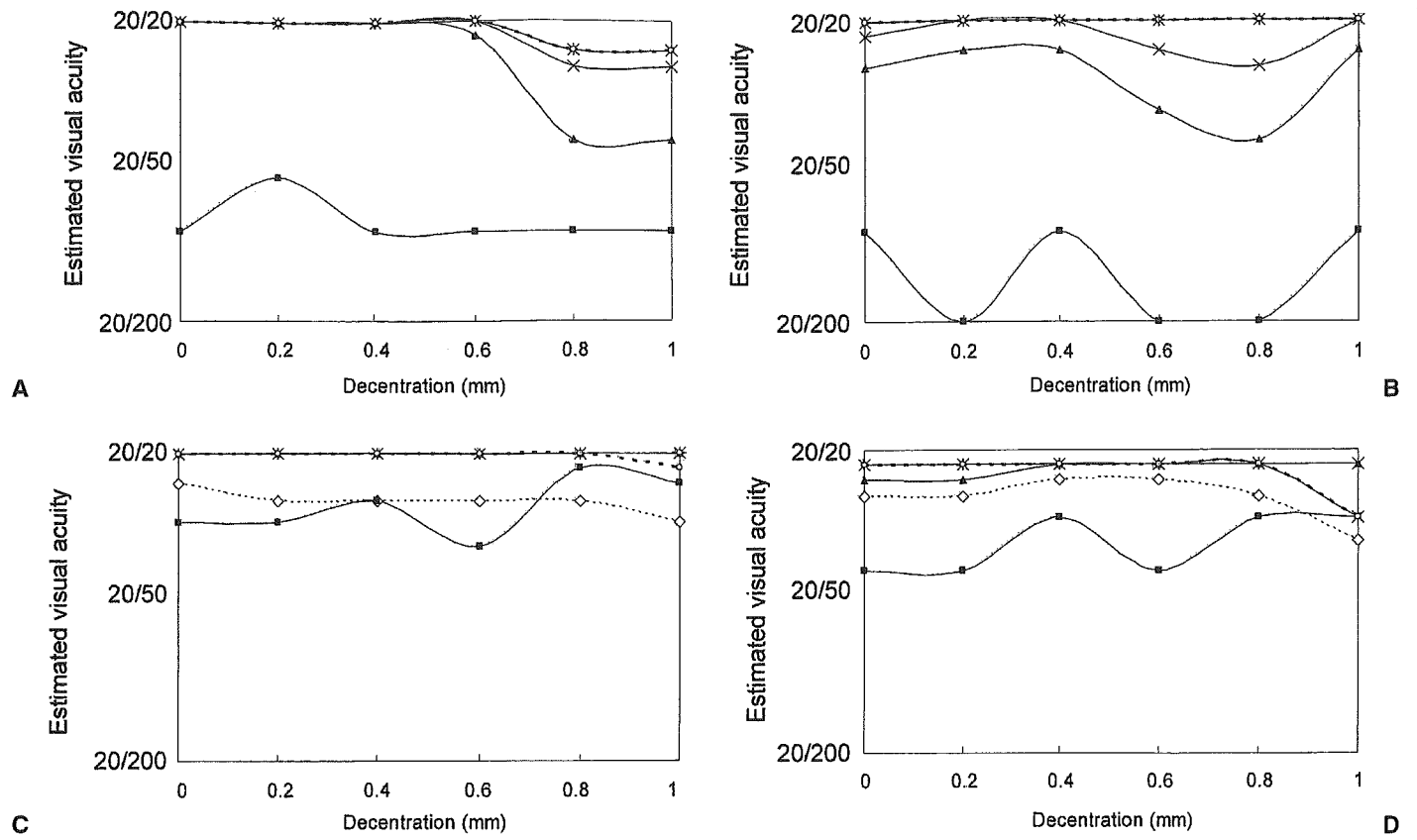

Figure 5A–D. Estimated visual acuities (VAs) derived from simulated retinal images. **A** Monofocal, φ = 3 mm; **B** monofocal, φ = 4 mm; **C** multifocal, φ = 3 mm; and **D** multifocal, φ = 4 mm. The estimated VAs are lower than 0.1 at 0.4 m at all examined decentration distances with the monofocal IOL. The direction of decentration cannot be set in the water cell. The VA worsens when the gap in the Landolt's ring is perpendicular to the direction of the IOL decentration. ---◇---, 0.4 m; —■—, 1 m; —▲—, 2 m; —✕—, 3 m; —✳—, 4 m; ---○---, 5 m.

tration increased. The decreased contrast was more noticeable through the 4-mm aperture than through the 3-mm aperture; however, the loss was small either way.

With the multifocal IOL, some loss of image contrast occurred at all distances except at 0.4 m, compared with the monofocal IOL; however, the images of the Landolt's rings were recognizable under almost all conditions. The image quality was worst at 1 m. Blurring of the image increased as the decentration increased, especially at intermediate and near distances with the 4-mm aperture. However, image degradation due to decentration generally did not seem to be a major problem with either IOL when considering retinal image quality.

Figure 5 shows the estimated VAs derived from simulated retinal images. The estimated VAs were lower than 0.1 at 0.4 m with a monofocal IOL under any decentration condition (data not shown, Fig. 5A, B); however, they were over 0.4 with a multifocal IOL (Fig. 5C, D). Because the direction of decentration cannot be preset in the water cell, the VA at each distance worsened when the gap of the Landolt's ring was perpendicular to the decentration, although the VA was not affected when the gap was parallel to the decentration. This may indicate that the estimated VA sometimes increased and decreased as decentration increased at each distance.

Discussion

In this study, the retinal images in eyes with a monofocal IOL and a refractive multifocal IOL with and without decentration were simulated objectively using our visual simulation system. The results showed that the effect of decentration on optical performance of a monofocal and a multifocal IOL is not itself great.

There have been several studies on the effect of IOL decentration on retinal image quality with monofocal IOLs and multifocal IOLs.[23–26] Regarding monofocal IOLs, Atchison[23,24] described the effect of IOL decentration on postoperative refractive error and the optimal shape. In the study, the postoperative refractive changes were presented in the form of graphs and spot diagrams without numerical values. Korynta et al.[25] analyzed the influence of various combinations of decentration and tilt on postoperative refractive error using ray tracing, and reported that IOL decentration and/or tilt causes myopic shift, oblique astigmatism, and

lateral shift of focus. Kozaki and Takahashi[26] reported the effect on peripheral images when planoconvex, biconvex, and meniscus IOLs were decentered 1 or 2 mm from the pupil center and showed that retinal image defocusing became more severe as IOL decentration and the angle of the incident light rays increased, probably because of astigmatism, coma, and field curvature. In clinical cases, Hayashi et al.[21] reported that no significant association existed between IOL decentration or tilt and log minimum angle of resolution VAs at 5.0, 3.0, 2.0, 1.0, 0.7, 0.5, and 0.3 m in eyes with a monofocal IOL without complication, although the amount of decentration was small (0.33 ± 0.38 mm).

Compared with these previous evaluation methods, our system has two advantages. One is that it can simulate retinal images in eyes with an IOL under conditions that resemble the actual clinical environment, where the incident angle to an IOL from the photographic lens is set to the same incident angle from the cornea in a human eye. Another advantage is that the system can simulate the retinal images with an IOL that cannot be calculated by a ray-tracing method owing to a lack of detailed optical data about the IOL, such as with the multifocal IOL used in this study.

Our results showed that the images with a monofocal IOL are minimally affected by decentration at 4 and 5 m; however, at 2 and 3 m, the image contrast slightly decreased with increased decentration. The simulation of VAs with a monofocal IOL supports these observations and showed that VAs are minimally affected by decentration up to 0.6 mm (Fig. 5A, B); however, the VAs slightly decreased by decentration over 0.6 mm at 2 and 3 m. The simulated VA somehow improved with 1-mm decentration compared with less decentration at 1, 2, and 3 m with a 4-mm aperture (Fig. 5B), which seemed to be the result of setting when the direction of the IOL decentration was almost parallel to the direction of the gap in the Landolt's ring.

The optical performance of the AMO Array refractive multifocal IOL is theoretically minimally affected by decentration because of its concentric five-zone optical design; however, its actual performance when the lens is decentered is unknown. Therefore, it is difficult to determine whether the multifocal IOL should be implanted when a minor intraoperative complication occurs that may result in decentration, such as a tear in the continuous circular capsulotomy (CCC). Hayashi et al.[21] previously reported that increased decentration is associated with decreased far and intermediate VAs; that is, decentration of 0.7 mm or greater substantially decreases the distance VA, and decentration of 0.9 mm is the maximal allowable limit in an eye with a multifocal IOL.[21]

In our results with a multifocal IOL, there was some decrease in image contrast at all distances except for 0.4 m compared with the monofocal IOL with or without decentration; however, optotype images were recognizable under all conditions. The visual simulation and estimated VA showed that the images were not greatly affected by decentration with the 3- and 4-mm aperture, except for the case with 1.0 mm decentration at far (4–5 m) and near (0.4 m) with the 4-mm aperture. The major distance focus zone of the AMO Array IOL is in the central 2.1-mm diameter. Because the aperture diameters used in this study were 3 and 4 mm, almost the entire central distance region must be exposed even when decentration reaches 1 mm. Therefore, the quality of the distance image might not be affected greatly by decentration up to 1 mm. However, the near-focus zone of the AMO Array IOL is in the zones between 2.1 and 4.6 mm, so the useful near-focus zone decreases when decentration occurs. These changes result in degradation of the image quality at near focus, especially with the 4-mm aperture, although degradation of the image quality would not be caused simply by obstruction of this region but by other optical factors such as astigmatism, coma, and field curvature generated by decentration of the optics.

In summary, our results using a new visual simulation system suggest that up to 1.0 mm of decentration of either monofocal and multifocal IOLs may not greatly affect the quality of vision. In clinical cases, over 1 mm of IOL decentration rarely occurs without major complications, so the effect of decentration on retinal images should not cause undue concern for an IOL implantation with a minor complication such as a tear in the CCC. However, we should always take decentration into consideration because the minor differences reported in this study might prove to be of greater importance in some circumstances, such as under conditions of reduced visibility, or with the newly designed IOL having a fixed amount of negative spherical aberration (Tecnis Z9000, Pharmacia, Groningen, The Netherlands), in which small differences in image quality become more important.

References

1. Ohnuma K, Shiokawa Y, Hirayama N, et al. Eye model for observing the images constructed by IOLs. Chin J Optom Ophthalmol 2000;12:332–325.
2. Pieh S, Marvan P, Lackner B, et al. Quantitative performance of bifocal and multifocal intraocular lenses in a model eye. Point spread function in multifocal intraocular lenses. Arch Ophthalmol 2002;120:223–238.
3. Portney V. Optical testing and inspection methodology for modern intraocular lenses. J Cataract Refract Surg 1992;18:607–613.
4. Lang A, Portney V. Interpreting multifocal intraocular lens modulation transfer functions. J Cataract Refract Surg 1993;19:505–512.
5. Artal P, Marcos S, Navarro R. Through focus image quality of eyes implanted with monofocal and multifocal intraocular lenses. Opt Eng 1995;34:772–779.
6. Korynta J, Bok J, Cendelin J, et al. Computer modeling of visual impairment caused by intraocular lens misalignment. J Cataract Refract Surg 1999;25:100–105.
7. El-Maghraby A, Marzouky A, Gazayerli E, et al. Multifocal versus monofocal intraocular lenses: visual and refractive comparisons. J Cataract Refract Surg 1992;18:147–152.
8. Steinert RF, Post CT Jr, Brint SF, et al. A prospective, randomized, double-masked comparison of a zonal-progressive multifocal intraocular lens and a monofocal intraocular lens. Ophthalmology 1992;99:853–860.
9. Negishi K, Nagamoto T, Hara E, et al. Clinical evaluation of a five-zone refractive multifocal intraocular lens. J Cataract Refract Surg 1996;22:110–115.

10. Negishi K, Bissen-Miyajima H, Kato K, et al. Evaluation of a zonal-progressive multifocal intraocular lens. Am J Ophthalmol 1997;124:321–330.
11. Pervical SPB, Setty SS. Prospectively randomized trial comparing the pseudoaccommodation of the AMO ARRAY multifocal lens and a monofocal lens. J Cataract Refract Surg 1993;19:26–31.
12. Steinert RF, Aker BL, Trentacost DJ, et al. A prospective comparative study of the AMO ARRAY zonal-progressive multifocal silicone intraocular lens and a monofocal intraocular lens. Ophthalmology 1999;106:1243–1255.
13. Jacobi PC, Konen W. Effect of age and astigmatism on the AMO Array multifocal intraocular lens. J Cataract Refract Surg 1995;21:556–561.
14. Revalico G, Paretin F, Baccara F. Effect of astigmatism on multifocal intraocular lenses. J Cataract Refract Surg 1999;25:804–807.
15. Hayashi K, Hayashi H, Nakao F, Hayashi F. Influence of astigmatism on multifocal and monofocal intraocular lenses. Am J Ophthalmol 2000;130:477–482.
16. Dick HB, Krummenauer F, Schwenn O, et al. Objective and subjective evaluation of photic phenomena after monofocal and multifocal intraocular lens implantation. Ophthalmology 1999;106:1878–1886.
17. Koch DD, Samuelson SW, Haft EA, Merin LM. Pupillary size and responsiveness. Implications for selection of a bifocal intraocular lens. Ophthalmology 1991;98:1030–1035.
18. Koch DD, Samuelson SW, Villarreal R, et al. Changes in pupil size induced by phacoemulsification and posterior chamber lens implantation: consequences for multifocal lenses. J Cataract Refract Surg 1996;22:579–584.
19. Revalico G, Baccara F, Bellavitis A. Refractive bifocal intraocular lens and pupillary diameter. J Cataract Refract Surg 1992;18: 594–597.
20. Yang HC, Chung SK, Baek NH. Decentration, tilt, and near vision of the Array multifocal intraocular lens. J Cataract Refract Surg 2000;26:586–589.
21. Hayashi K, Hayashi H, Nakao F, Hayashi F. Correlation between pupillary size and intraocular lens decentration and VA of a zonal-progressive multifocal lens and a monofocal lens. Ophthalmology 2001;108:2011–2017.
22. Campbell FW, Green DG. Optical and retinal factors affecting visual function. J Physiol 1965;181:576–593.
23. Atchison DA. Refractive errors induced by displacement of intraocular lenses within the pseudophakic eye. Optom Vis Sci 1989;66:146–152.
24. Atchison DA. Optical design of intraocular lens. III. On-axis performance in the presence of the lens displacement. Optom Vis Sci 1989;66:671–681.
25. Korynta J, Bok J, Cendelin J. Changes in refraction induced by changes in intraocular lens position. J Refract Corneal Surg 1994; 10:556–564.
26. Kozaki J, Takahashi F. Theoretical analysis of image defocus with intraocular lens decentration. J Cataract Refract Surg 1995;21: 552–555.

OPTICAL REVIEW Vol. 13, No. 2 (2006) 1–6

Reconstruction of the Point-Spread Function of the Human Eye Using a New Phase-Retrieval Algorithm

Yukio IIDA, Masahiro SHIBUTANI[1], Katsuhiko KOBAYASHI[1], Kazuhiko OHNUMA[2], Yoichi MIYAKE[2] and Toru NODA[3]

Graduate School of Science and Technology, Chiba University, 1-33 Yayoi-cho, Inage-ku, Chiba 263-8522, Japan
[1]*Topcon R&D Center, Tokyo, 75-1 Hasunuma-cho, Itabashi-ku, Tokyo 174-8580, Japan*
[2]*Faculty of Engineering, Chiba University, 1-33 Yayoi-cho, Inage-ku, Chiba 263-8522, Japan*
[3]*National Hospital Organization Tokyo Medical Center, 2-5-1 Higashigaoka, Meguro-ku, Tokyo 152-8902, Japan*

(Received October 3, 2005; Accepted December 28, 2005)

The double-pass method is thought to obtain the point spread function (PSF) in human eyes based on two techniques: the symmetric double-pass method using the same pupil size and the asymmetric double-pass method using a different pupil size. The symmetric double-pass method provides autocorrelation of the retinal PSF and, thus, the modulation transfer function. The asymmetric double-pass method provides low-frequency partial-phase information and the partial phase-retrieval algorithm is applied to obtain the complete-phase information, and to estimate the PSF. The partial phase-retrieval algorithm is based on the iteration method proposed by Fineup and Kowalczyk and requires a lengthy computation. In this study, we propose a new high-speed phase-retrieval algorithm based on the property that the real and imaginary parts of optical transfer functions (OTFs) continuously change in value.

Key words: double-pass point spread function, phase-retrieval algorithm, human eye, one-dimensional simulation

1. Introduction

Refractive surgeries, i.e., intraocular lens implantation and laser *in situ* keratomileusis, are gaining increasing popularity. However, even when good visual acuity is attained after the surgeries, some patients complain about, for example, a decrease in contrast. Ocular functions such as visual acuity and contrast can be derived objectively by using patients' ocular point spread function (PSF), which allows clinicians to objectively understand the optical performance.

The double-pass method has been proposed to obtain the PSF in human eyes based on two techniques: the symmetric double-pass method using the same pupil size and the asymmetric double-pass method using a different pupil size as reported previously.[1–8]

The symmetric double-pass method provides autocorrelation of the retinal PSF and, thus, the modulation transfer function (MTF). The asymmetric double-pass method provides low-frequency partial-phase information, and the partial phase-retrieval algorithm is applied to obtain the complete-phase information and to estimate the PSF. The partial phase-retrieval algorithm is based on the iteration method of Fineup and Kowalczyk,[9,10] and the algorithm requires multiple Fourier transformations because it calculates in the space and frequency domain alternately. As a result, the computational time is lengthy. The algorithm used in the current study does not use the characteristics of optical transfer function (OTF). The algorithm starts the calculation in the correct low-frequency partial phase, the high-frequency random initial phase, and the correct MTF. The algorithm seeks the PSF, the value of which exists in limited space without a negative value.

Another algorithm that uses the property of OTF is available. We identified the property of the changes in value of the real and imaginary parts of the OTF through one-dimensional computer simulation. The value of the real part of the OTF at 0 spatial frequency is 1 and it decreases and increases continuously in a wave-like fashion. The value of the imaginary part of OTF at the 0 spatial frequency is 0 and it increases or decreases continuously in a wave-like fashion. Therefore, the high-frequency partial phase can be extrapolated because the real and the imaginary parts of the OTF continuously change in value. This algorithm does not include a calculation of Fourier transform and requires a shorter calculation time. In this study, we show the efficiency and the usefulness of the proposed algorithm through one-dimensional simulation.

2. Optical System and Phase Retrieval

The schematic diagram of the optical system for the double-pass method is shown in Fig. 1. The light beam emitted by the point light source passes through a collimating lens and an artificial incident pupil and reaches the subject's eye. The artificial incident pupil restricts the diameter of the incident beam. The light beam reflected from the subject's retina passes through the artificial exit pupil and a second lens forms an aerial image on a charged couple device (CCD) array.

In the symmetric double-pass method, the diameter of the artificial incident pupil is the same as the diameter of the artificial exit pupil. With the asymmetric double-pass method, the diameter of the artificial incident pupil is smaller (less than 1.5 mm) than the diameter of the artificial exit pupil.

The algorithm for obtaining the MTF and the low-frequency partial phase transfer function (PTF) is as follows.[7] The images $i_D(x)$ on the CCD array obtained by

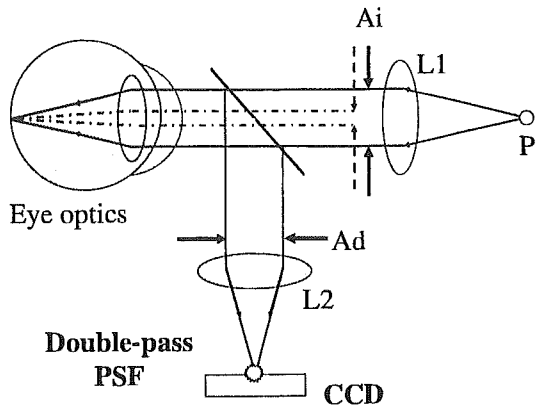

Fig. 1. Diagram of the optical system for the double-pass method. P: point source; L1 and L2: lens; Ai: artificial incident pupil; Ad: artificial exit pupil.

the symmetric double-pass method are related to the retinal image (ocular single-pass PSF) through an autocorrelation operation as follows:

$$i_D(x) = s_D(x) \otimes s_D(-x), \tag{1}$$

where $s_D(x)$ is the PSF for a pupil with diameter D, x is a two-dimensional spatial variable, and $\otimes$ indicates convolution. The Fourier transform of eq. (1) is

$$I_D(u) = (S_D(u))^2, \tag{2}$$

where $S_D(u)$ is the MTF of the eye for pupil diameter D and u is a two-dimensional spatial-frequency variable. The ocular MTF $S_D(u)$ is obtained from eq. (2).

The images $i_d(x)$ obtained using the asymmetric double-pass method are related to the retinal image through a convolution operation as follows:

$$i_d(x) = s_d(x) \otimes s_D(-x), \tag{3}$$

where $s_d(x)$ is the near-diffraction limited ocular PSF for pupil diameter (d) of the incident artificial pupil that is similar to an Airy pattern. The Fourier transform of eq. (3) is

$$I_d(u) = S_D(u)C_d(u)\exp[-iF_D(u)], \tag{4}$$

where $C_d(u)$ is the Fourier transform of $s_d(x)$, $C_d(u)$, and $I_d(u)$, and they are limited to the cutoff frequency u_d that corresponds to the small artificial incident pupil with diameter d. Because the PTF value of $C_d(u)$ is considered to be 0 in all spatial frequencies, the PTF is derived in low spatial frequency $[0, u_d]$ as follows:

$$F_d(u) = \tan^{-1}(\mathrm{Im}[I_d(u)]/\,\mathrm{Re}[I_d(u)]). \tag{5}$$

The algorithm for phase retrieval at the higher spatial frequency is as follows. The random values are added to the higher spatial frequency over u_d and the temporary PTF is constructed. The first-step PSF is obtained by the inverse Fourier transform of the combination of the correct MTF and the temporary PTF. The first-step PSF includes the negative value and exists in an unexpectedly wide area. The negative value of the first-step PSF is changed to a positive value or 0.

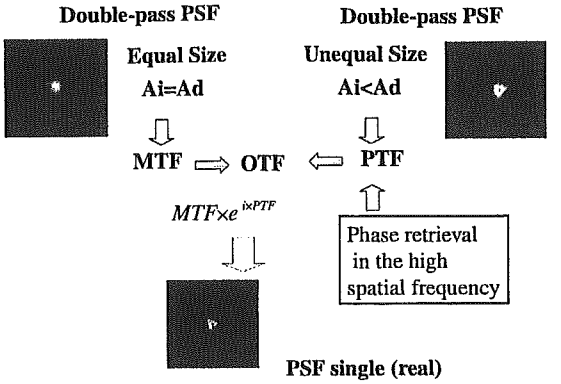

Fig. 2. Estimation of single-pass PSFs using the correct MTF and the PTF recovered by the phase-retrieval algorithm.

In addition, the values that lie outside of the expected area are changed to 0. By Fourier transform of the modified PSF, the second-step OTF that has a different value for MTF is obtained. After the MTF of the second-step OTF is changed to the correct MTF, the second-step PTF is calculated by inverse Fourier transform of the modified second-step OTF. This iteration process is performed repeatedly until the difference between the nth-step MTF and the correct MTF becomes small. However, the PTF is difficult to obtain with the small MTF value. Iglesias *et al.* reported a new method[7] that can solve this problem. Finally, the single-pass PSF is estimated using the correct MTF and the nth-step PTF (Fig. 2).

3. Property of OTF Value

The algorithm of the phase-retrieval method described previously does not use the changes in the OTF values from 0 to high spatial frequency. We observed the feature that exists in the change in the values of the real and imaginary parts of the OTFs through one-dimensional computer simulation. The tested OTFs were calculated from the wavefront aberrations expressed by the Zernike polynomial up to the fourth order, changing the coefficient that usually is seen. The one-dimensional wavefront is represented as follows:

$$g(x) = ax^4 + bx^3 + cx^2 + dx + e. \tag{6}$$

The four examples in which the PSFs for the four different wavefronts are analyzed are shown in Fig. 3, where the solid black line indicates the MTF, and the real and the imaginary parts of the OTF are represented by the dark gray line and the light gray line, respectively.

Figures 4 and 5 show the PTF and the primary differentiation of the real part of OTF in the case of example (1) in Fig. 3.

The MTF shown in examples (2) and (3) in Fig. 3 starts at 1 at the 0 spatial frequency, decreases, and does not change continuously. In addition, the large change in the value from plus (or minus) π to minus (or plus) π in the PTF is seen in Fig. 4. However, the real part of the OTFs has a value of 1 at spatial frequency 0, decreases continuously as the spatial

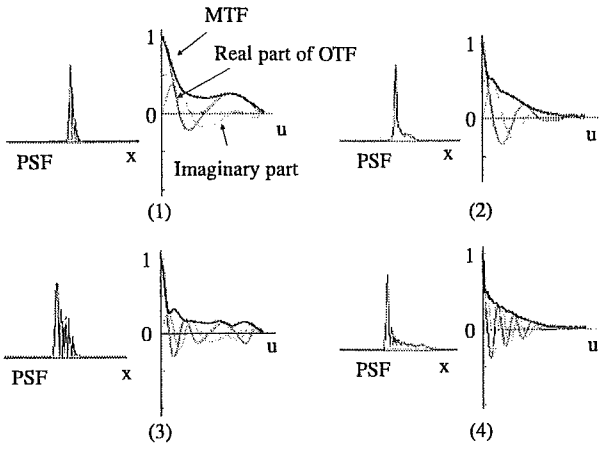

Fig. 3. Four examples of one-dimensional PSFs. Solid black line: MTF; dark gray line: real part of the OTF; light gray line: imaginary part of OTF; (1) wavefront $g(x) = 0x^4 + 0.5x^3 + 0.0x^2 + 0.0x + 0.0$; (2) wavefront $g(x) = 0.4x^4 + 0.5x^3 + 0.3x^2 + 0.1x + 0.0$; (3) wavefront $g(x) = 0.0x^4 + 1.2x^3 + 0.0x^2 + 0.0x + 0.0$; (4) wavefront $g(x) = 0.2x^4 + 1.2x^3 + 1.5x^2 + 0.1x + 0.0$.

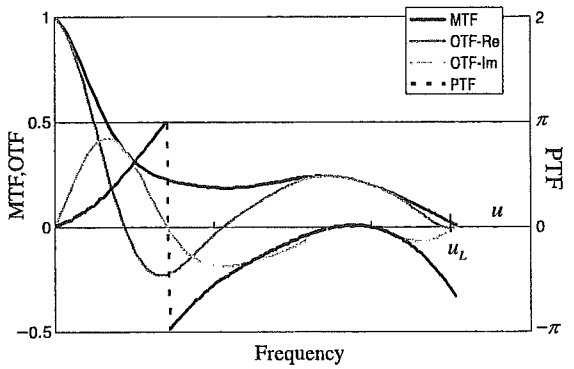

Fig. 4. Example of MTF and OTF obtained from the one-dimensional wavefront: $g(x) = 0x^4 + 0.5x^3 + 0.0x^2 + 0.0x + 0.0$. OTF-Re: real part of the OTF; OTF-Im: imaginary part of OTF.

frequency increases, and changes in a wave-like fashion of damped oscillation. Moreover, the imaginary part of the OTFs has a value of 0 in 0 spatial frequency, increases or decreases continuously as the spatial frequency increases, and changes in a wave-like fashion. In addition, the primary differentiation of the real part of OTF in Fig. 5 shows that the real part of OTF does not change suddenly. The imaginary part of OTF has the same feature.

As mentioned previously, the real and imaginary parts in the spatial frequency from 0 to u_d can be obtained by the double-pass method. Therefore, we consider that the higher frequency partial phase can be extrapolated by using the property that the real and the imaginary parts of OTFs continuously changes in value. The algorithm using this property is shown below.

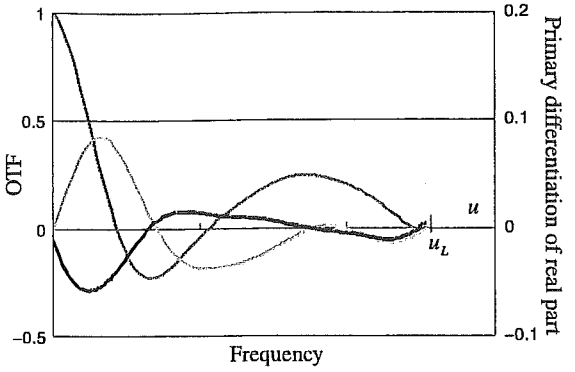

Fig. 5. Example of continuity. Black line: primary differentiation of the real part of the OTF; dark gray line: real part of the OTF; light gray line: imaginary part of OTF.

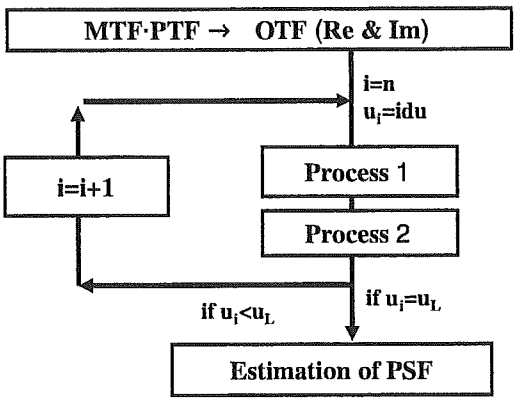

Fig. 6. The flow chart of the proposed algorithm.

4. New Algorithm

The proposed algorithm uses two properties. One is the continuous change of the real and imaginary parts of the OTF. The other is the definition of MTF that equals the square root of the real part squared plus the imaginary part squared. The proposed algorithm consists of two processes. The flow chart of this extrapolation process is shown in Fig. 6.

In the first process, the real and imaginary parts of the OTF are calculated from the MTF and the PTF. The values of the real and imaginary parts in the neighboring higher frequency then are separately predicted by process 1 described below. The predicted values then are modified to fit to the correct MTF in process 2 (Fig. 7). These processes are repeated from low to high spatial frequencies until the cutoff frequency of the large pupil (u_L). Finally, the real and imaginary parts in all frequencies are obtained and the ocular PSF is estimated.

4.1 Process 1

The values of the real and imaginary parts of OTF on the spatial frequency u_n are presumed separately using values

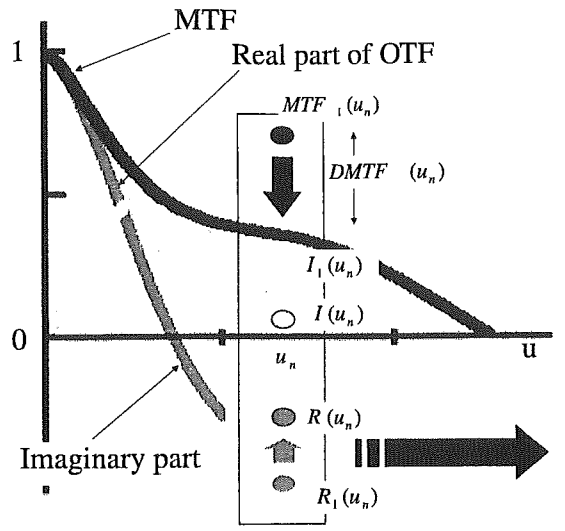

Fig. 7. Phase retrieval according to the proposed algorithm.

between 0 and u_{n-1}. The value of the real part $R_1(u_n)$ is presumed in process 1 as follows:

$$R_1(u_n) = R(u_{n-1}) + R_{ad}(u_{n-1}). \tag{7}$$

The spatial frequency is defined digitally as follows.

$$u_n = ndu, \tag{8}$$

where du is the amount of frequency change and n is the integer ($n = 0, 1, 2$). $R_{ad}(u_n)$ can be defined as follows:

$$R_{ad}(u_{n-1}) = \frac{\sum_{k=t}^{n-1} \langle R_1(u_k) - R_1(u_{k-1}) \rangle}{n-t}. \tag{9}$$

Here, we use the mean difference of the neighboring two values as $R_{ad}(u_n)$. k is selected in the region where the value of the real part increases or decreases monotonously. u_t is the lowest frequency in the continuous change. The other, the following formula seems to be available

$$R_{ad}(u_{n-1}) = R_1(u_{n-1}) - R_1(u_{n-2}). \tag{10}$$

However, the value of the real part includes slightly more noise, which leads to the unexpected $R_1(u_n)$. Therefore, $R_{ad}(u_n)$ of eq. (3) seems to be superior.

The values of the imaginary part $I_1(u_n)$ are presumed in a similar manner.

4.2 *Process 2*

$MTF_1(u_n)$ is calculated by using $R_1(u_n)$ and $I_1(u_n)$ obtained by process 1, as follows:

$$MTF_1{}^2(u_n) = R_1{}^2(u_n) + I_1{}^2(u_n). \tag{11}$$

Here $MTF_1(u_n)$ must be the correct MTF ($MTF_{cor}{}^2(u_n)$) obtained by the symmetrical double-pass method.

However, the difference between the correct MTF and the derived $MTF_1{}^2(u_n)$ exists and is defined as follows:

$$DMTF(u_n) = MTF_{cor}{}^2(u_n) - MTF_1{}^2(u_n). \tag{12}$$

The difference is distributed to the real and the imaginary parts, respectively, according to the following formulas:

$$DR(u_n) = DMTF(u_n) \times ratioR(u_n), \tag{13}$$

$$DI(u_n) = DMTF(u_n) \times ratioI(u_n), \tag{14}$$

where $DR(u_n)$ and $DI(u_n)$ are the amounts of distribution for the real and the imaginary parts, respectively.

The ratios for distribution are expressed as follows:

$$ratioR(U_n) = \frac{R_1{}^2(U_n)}{R_1{}^2(U_n) + I_1{}^2(U_n)}, \tag{15}$$

$$ratioI(U_n) = \frac{I_1{}^2(U_n)}{R_1{}^2(U_n) + I_1{}^2(U_n)}. \tag{16}$$

This is based on the idea that it seems to be better to decide the distribution ratio according to the magnitude of the value.

Finally, the real and imaginary parts are determined as follows:

$$R(u_n) = k\sqrt{R_1{}^2(u_n) + DR(u_n)}, \tag{17}$$

$$I(u_n) = k\sqrt{I_1{}^2(u_n) + DI(u_n)}, \tag{18}$$

where sign k is defined as:

$$k = \begin{cases} +1 & \text{if } R_1(u_n) \text{ or } I_1(u_n) > 0 \\ 0 & \text{if } R_1(u_n) \text{ or } I_1(u_n) = 0 \\ -1 & \text{if } R_1(u_n) \text{ or } I_1(u_n) < 0 \end{cases}. \tag{19}$$

The value of k is determined by whether the change increases or decreases.

5. Computer Simulation and Results

The simulation using the proposed algorithm was performed as follows. Many wavefronts were prepared and the PSFs were calculated. By Fourier transform, MTF and PTF were obtained for each PSF. The values of the high frequency of PTF were set to 0. The values of PTF in the high spatial frequencies were reproduced using the proposed algorithm, and PSF was estimated. Finally, the estimated PSF was compared with the original PSF with the correct value the high spatial frequency to confirm the performance of the proposed algorithm.

5.1 *Experimental procedure*

The two-dimensional PSF is calculated by the following equations:

$$F(u,v) = \iint \exp\left[-i\frac{2\pi}{\lambda} w(x,y)\right] \times \exp\left[-i\frac{2\pi}{\lambda}(ux, vy)\right] dxdy, \tag{20}$$

$$PSF(x,y) = F(u,v) \times F^*(u,v), \tag{21}$$

where $w(x,y)$ is the wavefront represented by the Zernike polynomial. Here, eqs. (20) and (21) become one dimensional as follows:

$$F(u) = \int \exp\left[-i\frac{2\pi}{\lambda} g(x)\right] \exp\left[-i\frac{2\pi}{\lambda}(ux)\right] dx \tag{22}$$

$$PSF_{ori}(x) = F(u) \times F^*(u), \tag{23}$$